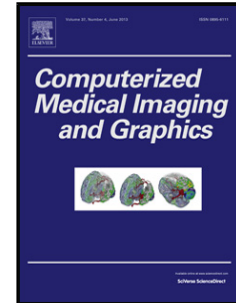# Accepted Manuscript

Title: Atlas-based Rib-Bone Detection in Chest X-rays

Author: Sema Candemir Stefan Jaeger Sameer Antani Ulas Bagci Les R. Folio Ziyue Xu George Thoma

Please cite this article as: Sema Candemir, Stefan Jaeger, Sameer Antani, Ulas Bagci, Les R. Folio, Ziyue Xu, George Thoma, Atlas-based Rib-Bone Detection in Chest X-rays, <![CDATA[*Computerized Medical Imaging and Graphics*]]> (2016), http://dx.doi.org/10.1016/j.compmedimag.2016.04.002

Atlas-based Rib-bone Detection in Chest X-rays

- Automated system which detects the rib-bones in patient chest X-rays
- In addition to traditional atlas, two alternative atlases usage
- Successfully rib-bone localization for patient X-rays
- Comparable results with the state-of-the-art algorithm
- Good results on challenging X-rays: successfully addressing the rib-shape variance between patients, and number of visible rib bones due to inhale condition of the patient

Atlas-based Rib-Bone Detection in Chest X-rays

Sema Candemir[1], Stefan Jaeger[1], Sameer Antani[1], Ulas Bagci[3], Les R. Folio, Ziyue Xu[2], George Thoma[1]

[1]*Lister Hill National Center for Biomedical Communications U.S. National Library of Medicine, National Institutes of Health, Bethesda, MD, USA*
[2]*Radiology and Imaging Sciences, National Institutes of Health, Bethesda, MD, USA*
[3]*Center for Research in Computer Vision, University of Central Florida, Orlando, FL, USA*

Abstract

This paper investigates using rib-bone atlases for automatic detection of rib-bones in chest X-rays (CXRs). We built a system that takes patient X-ray and model atlases as input and automatically computes the posterior rib borders with high accuracy and efficiency. In addition to conventional atlas, we propose two alternative atlases: (i) automatically computed rib bone models using Computed Tomography (CT) scans, and (ii) dual energy CXRs. We test the proposed approach with each model on 25 CXRs from the Japanese Society of Radiological Technology (JSRT) dataset and another 25 CXRs from the National Library of Medicine CXR dataset. We achieve an area under the ROC curve (AUC) of about 95% for Montgomery and 91% for JSRT datasets. Using the optimal operating point of the ROC curve, we achieve a segmentation accuracy of 88.91 ± 1.8 % for Montgomery and 85.48 ± 3.3 % for JSRT datasets. Our method produces comparable results with the state-of-the-art algorithms. The performance of our method is also excellent on challenging X-rays as it successfully addressed the rib-shape variance between patients and number of visible rib-bones due to patient respiration.

Keywords: Chest X-rays, Rib bone extraction

1. Introduction

The National Library of Medicine has developed a portable chest X-ray (CXR) screening system to automatically detect the lung abnormalities in countries where health resources are constrained [1, 2, 3]. The system extracts the texture and shape properties of lung regions from CXR images, and identifies the abnormality using image processing and machine learning algorithms. On a typical CXR, the bone structures overlap with the lung tissue due to the 2D projection of the chest. The ribcage causes a cross-hatching pattern on the lung region, which misleads the texture analysis [4, 5, 6, 7]. A straightforward solution to this problem would be to extract textures only from the inter-costal regions. This strategy indeed increases the accuracy of normal/abnormal lung classification [5]. Another way to improve the texture analysis is to suppress the rib-bone by reducing the intensities for rib regions, and to work on soft-tissue-like images [8, 9, 7]. The soft-tissue-like images can be obtained by subtracting the rib region from the input X-ray. Automatic rib-bone extraction is not only useful for better texture analysis, but also useful for pediatric CXR screening where rib borders could be used to detect the rib abnormalities, such as rickets or neurofibromatosis [10]. Rib boundaries also need to be detected accurately in stereo radiography in order to reconstruct an accurate 3D rib-bone model [11].

Email address:
sema.candemir@nih.gov,stefan.jaeger@nih.gov,
sameer.antani@nih.gov, ulas.bagci@nih.gov,
les.folio@nih.gov, ziyue.xu@nih.gov,
george.thoma@nih.gov (Sema Candemir[1], Stefan Jaeger[1], Sameer Antani[1], Ulas Bagci[3], Les R. Folio, Ziyue Xu[2], George Thoma[1])

Rib-bone detection is challenging due to (i) spurious boundaries caused by overlapping anatomical structures, (ii) multiplicative noise and sampling artifacts during acquisition, and (iii) deformation of tissues and anatomical shape variations caused by disease. Rib border contrast is generally poor/low because of the similar intensity values at the rib boundaries and nearby tissues. In addition to these challenges, rib bone appearance varies between patients due to differences in bone mineral density, respiration, and body movement during X-ray capture. Fig 1 shows a typical rib shape variance across patients, as well as spurious boundaries.
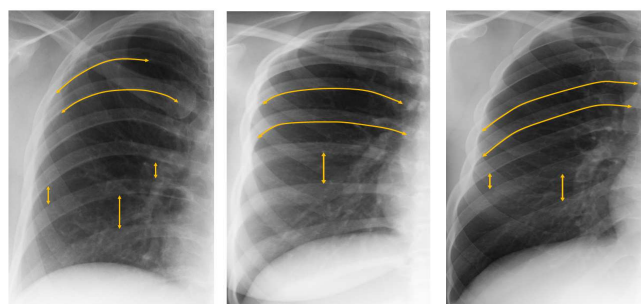

Figure 1: Example X-ray images of the right lung from different patients. The rib-bone structure (the bone curvature and interval between the bones) is different for each patient.

It has been shown in numerous studies that prior-information-based segmentation methods are more accurate than those without prior information [12, 13, 3, 14, 15]. One way to incorporate prior knowledge is to use a prototype 'at-

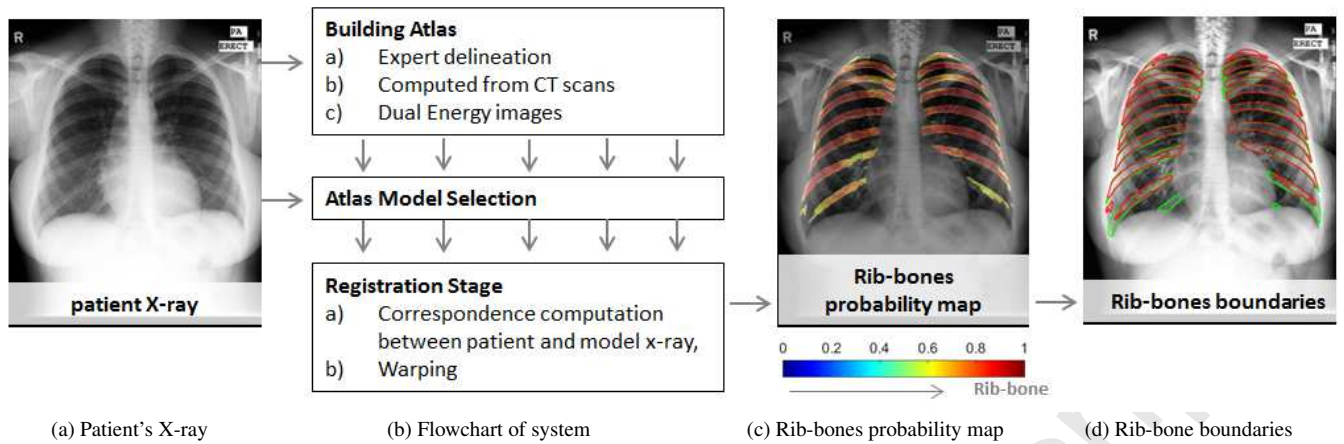(a) Patient's X-ray   (b) Flowchart of system   (c) Rib-bones probability map   (d) Rib-bone boundaries

Figure 2: The flowchart of the proposed method. (a) Patient's X-ray. (b) The main stages of the system: atlas building, model selection and atlas registration. (c) The computed probability map of rib-bones overlapped on the patient's X-ray. The probability map is normalized between 0 and 1. The red color indicates the high probability of being rib-bone. (d) The rib-bone boundaries computed by thresholding the probability maps. The red contour is the computed boundary and the green contour is the reference boundary.

las'. Herein, we investigated the use of atlases for automated rib-bone extraction from CXRs. An illustrative flowchart of the proposed approach is shown in Figure 2. An atlas, in the context of this work, is defined as a set of model X-ray images and their corresponding rib-bone boundaries. The models are constructed via three methods: i) X-ray image with manually delineated rib-bone boundaries (Fig 3.a); ii) simulated X-ray and rib-bone model image generated from Computed Tomography (CT) scans (Fig 3.b); and iii) CXRs obtained from a dual energy scanner (Fig 3.c). The atlas is registered to the patient X-ray, yielding a transformation for each pixel, which allows the corresponding atlas rib mask to be transformed and treated as segmentation for the rib-bone of the patient.

We summarized previous studies and our contribution in Section 2. The datasets used in our study are listed in Section 3.1. The methodology is described in Section 3.2, which includes the atlas construction, model selection, and atlas registration. We provide the experimental results in Section 4. We discuss and conclude the study in Section 5.

2. Literature Review

Atlas-based Segmentation. In recent years, various research efforts have been conducted for model-based segmentation methods, such as active shape models [16] and active appearance models [17]. Similarly, the use of atlas priors have broad applications in medical image segmentation, especially in computing the complex boundaries of anatomical organs such as the heart [12] or brain [13, 18, 19]. A single atlas model could be used as the segmentation of the target image, but some studies have reported that a multi-atlas approach yields higher accuracy than single-atlas segmentation methods [20, 14]. In the multi-atlas approach, several atlas models are registered to the target image. The combination of all registered atlas models can be used as the final segmentation [14, 21, 22, 15, 23]. Studies showed that a selection of a specific subset of atlas models
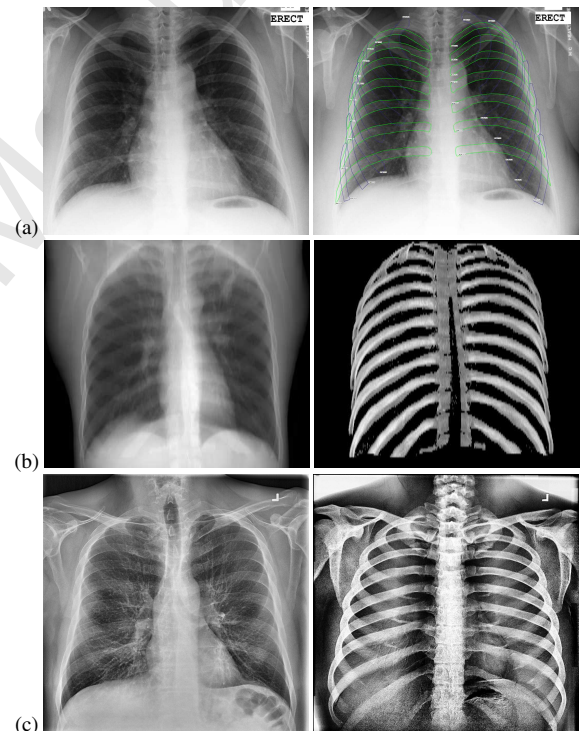

Figure 3: Example members of our atlas containing (a) the model X-ray and its manually delineated rib-bone model, (b) simulated X-ray and rib-bone model computed from CT, and (c) X-ray and corresponding enhanced bone images obtained from a dual-energy X-ray scanner.

for the target image produces more accurate segmentation results [3, 14, 15]. The registered atlas could be used as a prior for further segmentation stages [3, 24].

Rib Boundary Detection. Researchers have developed various methods for automated rib detection. The general approach is first extracting the rib pixels using an edge detection algorithm [25]. Then, the candidate rib pixels/lines are grouped into a complete rib boundary by applying a curve fit-

2

ting technique [26], using a voting approach such as Hough transform [10, 27], or applying a geometric model such as parabolas [28, 29, 30, 7] or ellipses [31]. Although extracting the rib borders with an edge detection algorithm is a well-known approach, these algorithms produce spurious edges at the apex of the lung due to overlapping bone structures. In addition, low rib contrast in the lower lung can cause problems. Applying geometric models can help infer missing rib boundaries; however, relying on a rigid model is not suitable for varying rib shapes among multiple patients (cf. Fig 1) and deformed ribs (e.g. in scoliosis cases [11]). Some authors use deformable models to cope with the shape variability [10, 32]. A recent effort for rib-bone detection is presented in [11], which uses oriented filtering and edge following with multiple-path branching. This algorithm addresses the large variability in rib bone shape. However, the method is a semi-automatic approach that requires user initialization for each rib in the target X-ray, which makes the whole process less efficient. Apart from the edge-based methods, some studies follow classification schemes to classify rib/non-rib pixels. For example, in [31], lower/upper margins of rib regions are classified by analyzing edge gradients and their orientations. In [33], pixels are classified using gray-scale and neighborhood structural information. In [34], rib-bones are extracted from CT images using Random Forest classifiers.

One of the aims of extracting the rib bones is suppressing the bones and obtaining soft-tissue-like images for better texture analysis. Although soft-tissue images can be obtained with dual-energy scanners, this imaging technology is newly developed, so a limited number of hospitals have access to this technology. Therefore, researchers proposed automatically simulated alternatives to produce soft-tissue images. For example in [8] the bone regions are computed by training an artificial neural network. In [9] the bone-like structures are extracted by applying regression filters learned from the training data. In [7], authors first delineate the rib-bone candidates with parabola curve fitting, and then the delineated ribs are suppressed using an unsupervised regression model which also takes into account the proximal thickness of bone.

Our Contribution. In this study, we used rib-bone atlases to automatically extract the patient rib-bone on conventional frontal CXRs. To the best of our knowledge, no study on atlas-based rib-bone detection has been previously reported. The proposed system chooses the most similar models in the atlas set and then registers them to the patient's X-ray. The average of all registered models constitutes the rib bone probability map for the patient's X-ray. In addition to manual delineation, we propose two alternative ways to build the rib-bone atlases: simulated models computed from CT images and bone images obtained from a dual energy scanner. The advantages of our detection system are: (i) The system automatically detects rib bones from conventional X-rays without any user interaction. (ii) The rib-bone models incorporate the anatomical knowledge of rib structures (e.g., spatial relations between rib bones). Therefore, the system takes into account the inter-rib spaces and fills the gaps between ribs using the information in the rib-models. (iii) Contrary to classical techniques, the texture-based registration

can cope with the large variation in rib shapes and curvatures.

3. Methods

3.1. Data

JSRT dataset is a set compiled by the Japanese Society of Radiological Technology (JSRT) [35]. It contains 247 CXRs, of which 154 X-rays have lung nodules, and 93 X-rays are normal with no nodules. All CXRs have a size of 2048×2048 pixels and a gray-scale color depth of 12 bits. The X-rays were captured using an analogue imaging system by exposing film that was later scanned into digital format [36]. The JSRT set is publicly available and has reference masks for clavicle bones, lung, and heart [36]. An expert manually labeled the rib-bone masks of 25 X-rays for our experiments serving as reference standards.

Montgomery dataset is a set from the Department of Health and Human Services, Montgomery County, Maryland, USA. The data set consists of 138 CXRs; 80 X-rays are normal and 58 X-rays are abnormal with manifestations of tuberculosis. The X-ray images are stored in 12-bit gray-scale with dimensions of 4020×4892. Since the X-rays were acquired using digital scanners, the images have much higher contrast; rib-bone edges are stronger and intensity variations are more heterogeneous compared to the JSRT dataset. The Montgomery dataset is publicly available for research [1, 3]. For our experiments, participating expert manually labeled the rib-bone masks of 25 X-rays serving as reference standards.

Belarus dataset is a set collected for a drug resistance study initiated by the National Institute of Allergy and Infectious Diseases, the United Institute of Informatics Problems of the National Academy of Sciences of Belarus, and the Republican Research and Practical Center for Pulmonology and Tuberculosis, Ministry of Health, Republic of Belarus [37]. The set contains both CXRs and chest CTs of 169 patients. Chest radiographs were taken using the KODAK Point-of-Care 260 system with 2248×2248 pixel resolution. CT scanning was performed by a GE LightSpeed Pro 16 scanner with a slice thickness of 2.5 mm and a number of axial slices varying from 100 to 160 depending on the region of interest [38]. Reference boundaries of the lung regions are available for each patient. We used the CT images of this dataset to build reference rib-bone boundaries.

NIH-Clinical Center-Dual Energy Images. The dual energy (DE) radiography involves taking two radiographs at different mean beam energies. The resulting radiographs highlight either the soft-tissue or bone structures. The DE CXRs used in this paper are routine CXRs obtained for clinical reasons using a GE Discovery XR656 digital radiography system (120 and 133 kVp).

3.2. Atlases

As rib-bone atlases, we used (i) conventional CXRs and manually delineated rib boundaries, (ii) simulated X-rays and rib models computed from CT scans, and (iii) X-rays from dual energy CXRs.

3

3.2.1. Manually delineated rib-bones

We selected 50 PA CXRs from the JSRT and Montgomery datasets and delineated the rib boundaries using the web-based labeling tool FireFly [39, 40], which offers precise drawing functionality and online labeling capabilities. Fig 3.a shows an example X-ray with manually delineated borders. In this example, the posterior ribs are marked in green while the anterior ribs are shown in blue. The manual boundaries are used as reference standard for quantitative analysis.

3.2.2. Simulated X-rays and corresponding rib-bone models

Manual delineation is a tedious process for rib borders, considering that most CXRs need at least 12 manual labels (six visible rib pairs). We propose an alternative rib-bone atlases computed from CT scans. The rib-bone models are constructed using CT scans, which is a simplified version of the study in [41]. For this task, we used the Belarus dataset. According to the Hounsfield scale in CT, bone has the highest radiodensity compared to other elements in tissue, ranging from +700HU to +3000HU (Hounsfield Unit). Based on this information, we assumed that the pixels with the maximum intensity at each column in the axial plane correspond to bone tissue. Therefore, we project the maximum intensity of each column in the axial plane to the coronal plane by

$$\mathbf{MIP}_{I_k} = < \max(I_k[c_i]) >, \quad \forall c_i \in I_k, \quad i = 1, 2, ...C, \quad (1)$$

where $\mathbf{MIP}_{I_k}$ is the maximum intensity projection vector of image I_k; I_k is the kth axial slice of CT scan; $I_k[c_i]$ is the intensity value of image I_k at i^{th} column.

We simulate the corresponding X-ray image with the same fashion by projecting the average intensity at each column in the axial plane to the coronal plane by

$$\mathbf{AIP}_{I_k} = < \text{avg}(I_k[c_i]) >, \quad \forall c_i \in I_k, \quad i = 1, 2, ...C, \quad (2)$$

where $\mathbf{AIP}_{I_k}$ is the average intensity projection vector of image I_k; I_k is the kth slice of CT scan; and $I_k[c_i]$ is the intensity value of image I_k at i^{th} column. We repeat the projection process for each axial slice, obtaining the simulated X-ray and rib-bone model in the coronal plane. In order to reduce the noise, we project the intensities only inside the thorax region. Fig 4 illustrates the rib-bone construction process from CT scans.

3.2.3. Dual Energy X-rays

As an alternative atlas model, we used tissue subtracted (bone) images obtained from dual energy scanner. We applied histogram equalization to increase the contrast between bone and non-bone pixels (Figure 3.c).

3.3. Atlas Selection

Registration is a computationally expensive process. Therefore, we registered only a subset of our atlas instead of registering the full atlas. It is generally difficult to compute an accurate mapping between images with large shape differences. In order to decrease the shape difference between the patient's X-ray and the atlas, we used a selection strategy that chooses the rib-models that are most similar to the patient's X-ray. The shape

similarity between the patient and the model X-rays are measured using the edge information of lung regions. The prominent edges in the lung regions are mostly caused by ribs. However, there are usually spurious edges which do not belong to rib bones. Therefore, before measuring the edge similarity, we applied bilateral filtering [42], which decreases the noise in the image but preserves the prominent edges. After filtering, we applied the Canny Edge detection algorithm [43] to obtain the edge map of an X-ray. Fig 5 shows the edge detection results on filtered X-rays. We measure the similarity of the edge maps of X-ray images using the equation

$$d(I_p^E, I_m^E) = \frac{1}{|I_p^E|} \sum_{x \in I_p^E, x' \in I_m^E} \min|x - x'| \quad (3)$$

where I_p^E is the binary edge image of the patient X-ray, I_m^E is the binary edge image of the model X-ray, x and x' are coordinates of edge pixels, and $|I_p^E|$ is the number of edge pixels in I_p^E.

The system computes the distance d between the edge map of the patient X-ray and the edge map of each X-ray in the atlas, and retrieves the most similar top-n rib-bone atlas models. After creating the subset, we registered the selected x-rays to the patient's x-ray to build a patient-specific rib-bone model.

3.4. Registration of Atlases

The aim of the registration stage is to build a rib-bone model for the patient X-ray using other patient X-rays with their corresponding rib-bone models. We employed a non-rigid registration method [44] that solves the registration process with a flow-based approach. The algorithm computed the corresponding pixels (the transformation mapping) between the models and the patient X-ray. Then, we aligned the rib-model to the patient X-ray by applying the transformation mapping. The registered model is used as the rib-bone model of the patient's X-ray. For the correspondence computation, the local regions are modeled with Scale Invariant Feature Transform (SIFT) [45]. The SIFT feature of a local region is the concatenation of the gradient orientation histograms of its sub-regions. To enhance the texture and rib contrast, histogram equalization is applied to chest X-rays before SIFT extraction. Once the SIFT features are computed for all atlas X-rays, the algorithm computes the pixel-to-pixel correspondences using the following objective function:

$$E(\mathbf{w}) = \sum_{\mathbf{p} \in \mathbf{P}} min(\|S_1(\mathbf{p}) - S_2(\mathbf{p} + \mathbf{w}(\mathbf{p}))\|, t)$$
$$+ \sum_{\mathbf{p}} (|u(\mathbf{p})| + |v(\mathbf{p})|)$$
$$+ \sum_{(\mathbf{p},\mathbf{q}) \in N} min(|u(\mathbf{p}) - u(\mathbf{q})|, d) + min(|v(\mathbf{p}) - v(\mathbf{q})|, d), \quad (4)$$

where P is the set of pixels in the X-ray; N is the spatial neighborhood set, S_1 and S_2 are the SIFT images in which each pixel is represented by a SIFT descriptor vector; $\mathbf{w}(\mathbf{p}) = (u(\mathbf{p}), v(\mathbf{p}))$ are the flow vectors at $\mathbf{p}$; t and d are the truncated thresholds. The minimization algorithm calculates the SIFT-flow $\mathbf{w}$ by optimizing the objective function. The first term of the objective
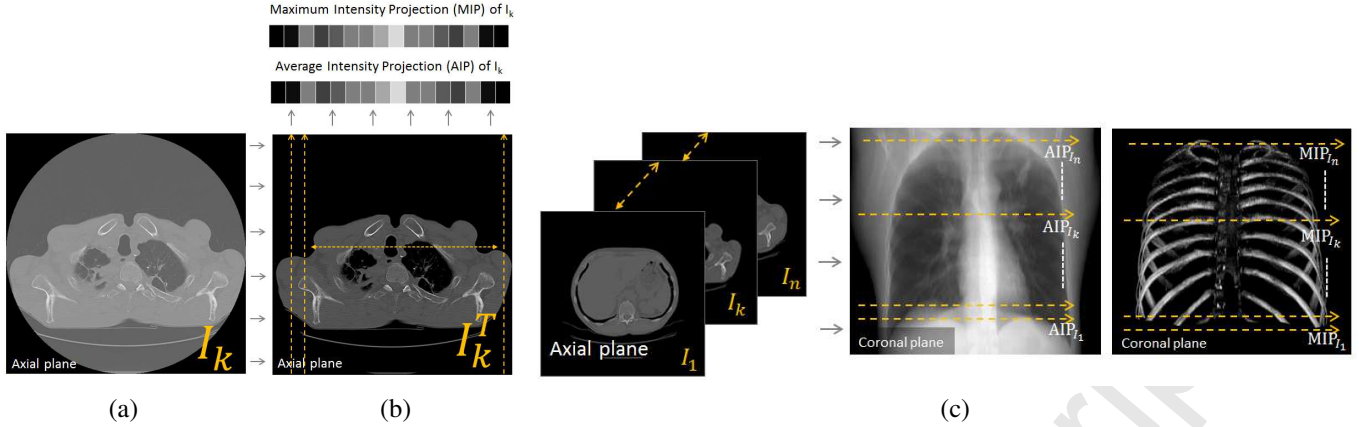
4

Figure 4: An illustration of the X-ray and rib-bone model simulation process. (a) An example slice (Image I_k) in the axial plane in a CT scan. (b) Algorithm thresholds the image I_k with +1300 HU (the threshold value is decided empirically) to obtain the approximate torso region image (I_k^T). The maximum and average intensity at each column of I_k^T is projected to the coronal plane. (c) Algorithm computes the Average Intensity Projection (AIP) and Maximum Intensity Projection (MIP) of all axial slices. Each AIP vector represents one image row of the simulated X-ray, and each MIP vector builds one row of the rib-bone model in the coronal plane.
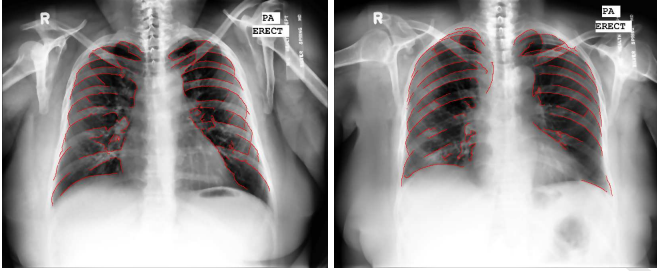

Figure 5: Canny Edge detection results for two filtered X-rays.

function forces the algorithm to match pixels according to their SIFT descriptors, with warping based on the registration flow vector $\mathbf{w}(\mathbf{p})$. The second term constrains the flow vectors to be as small as possible. The third term constrains the flow vectors of neighboring pixels to be similar. The SIFT-flow algorithm calculates corresponding matches for each pixel between two X-rays by solving the flow vectors $\mathbf{w}(\mathbf{p})$. The spatial shifts between corresponding matches define the transformation mapping for all pixels. We applied the transformation mapping by shifting each pixel in the atlas model according to the computed shift distance.

We repeated the registration stage for each of the top-n most similar X-rays in the atlas set. The final rib-bone model for the patient X-ray was built-up by using the mean of the top-ranked registered masks. The intensity value of each pixel in the rib-bone model for the patient X-ray is the probability that the pixel belongs to the rib bones (cf. Fig 6).

4. Experiments

4.1. Evaluation Strategy

One important challenge for medical image segmentation algorithms is to obtain a reference to validate the algorithm per-

formance and compare different methods. Generally, several experts are asked to delineate the borders, preferably multiple times. Then, the collection of expert markings are combined into one reference standard either taking the average of markings or employing a more sophisticated algorithm such as STAPLE (Simultaneous Truth And Performance Level Estimation) [46]. However, expert delineation is a tedious process, especially for rib borders considering that CXRs need at least 12 manual labels (for visible ribs). Therefore, currently available rib-bone detection studies suffer from a lack of standards and such algorithms have been tested on limited datasets. For example, the algorithm in [10] is tested only on 10 CXRs. In [33], researchers manually delineated the rib borders of 30 X-rays, and evaluated their algorithm on this set. Due to the lack of reference boundaries, some studies reported only subjective evaluations of an expert or of the authors themselves. For this study, we delineated the rib-bone boundaries of 50 CXRs, and each CXRs has only one reference standard.

There are 12 pairs of ribs in a normal human rib cage. Although the exact number depends on respiration, typically, six to nine rib pairs are visible in the lung area. The rib bones below the diaphragm are hardly visible in an CXR because of the abdomen shadow. Therefore, we define the lung area as the search area for ribs. To detect the lung area, we used a lung segmentation algorithm [3]. The resulting boundaries were compared with manual reference boundaries using Overlap = |TP|/(|FP| + |TP| + |FN|), Dice = 2|TP|/(2|TP| + |FN| + |FP|), Accuracy = (|TP| + |TN|)/(|TP| + |TN| + |FP| + |FN|), Sensitivity = |TP|/(|TP| + |FN|), Specificity = |TN|/(|TN| + |FP|) and Precision = |TP|/(|TP| + |FP|) where TP (true positives) represents correctly classified pixels, FP (false positives) represents pixels that are classified as rib but that are in fact background, FN (false negatives) represents pixels that are classified as background but that are in fact part of the ribs, and TN (true negatives) represents correctly classified non-pixels.

5

4.2. Rib-bone Probability Map

In this section, we report the performance of the proposed system with quantitative and qualitative evaluations of rib-bone probability maps. Given a patient X-ray, our system retrieves the top-n most similar X-rays in the atlas by comparing the edge maps of X-rays, and it then registers the selected models to the patient X-ray. The average of the registered models forms the rib-bone probability map in which the intensity of each pixel indicates its probability of being part of the rib-bone structure. Fig 6 shows an example computed probability map and its overlap on the X-ray image.
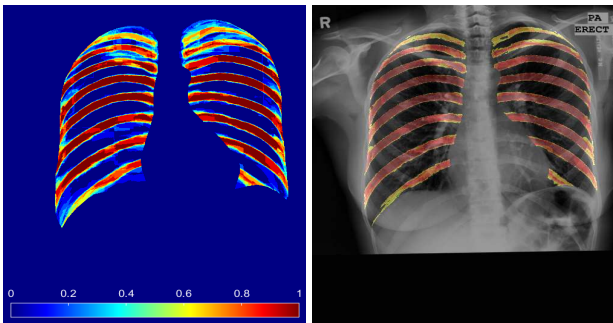

Figure 6: The probability maps and their overlap on X-rays.

As we described in Section 3.2, we use three types of atlas models: (i) conventional X-rays and manually-labeled boundaries, (ii) simulated X-rays and rib bone models computed from CT scans, and (iii) conventional X-rays and dual energy bone-tissue images. We tested the system performance with each model. Fig 7 shows computed probabilities with each atlas model for the same X-ray images. As can be seen from the overlapped figures, the algorithm assigns higher probabilities to rib regions than to intercostal areas. The visual results also show that the algorithm produces relatively less accurate boundaries at the bottom part of the lung. This is due to weak rib-bone edges in this region because of the lack of intensity difference between rib-bone and soft tissue.

The intensities of probability maps represent confidence values that we thresholded to obtain different operating points on the ROC curve. With a high threshold, high intensity values are classified as rib, producing high specificity and low sensitivity. On the other hand, with a low threshold, lower intensities will also be classified as rib. This will reduce the specificity of the model but increase its sensitivity. Figure 8 shows the ROC curves obtained for JSRT and Montgomery datasets, for manually delineated, simulated, and dual energy rib-bone models.

As an overall performance, we achieved an area under the ROC curve (AUC) of approximately 95% for Montgomery dataset and 91% for JSRT dataset (shown in Figure 8 and listed in Table 1). The curves show that the computed rib probabilities for the Montgomery set (blue curves) is better than the rib probabilities for the JSRT set (red curves). As we reported in Section 3.1, the JSRT set was captured using an analogue imaging system by exposing film that was later scanned into digital

Dataset	Models	AUC	opt. TP	opt. FP
JSRT	manually delineated	0.9105	0.7944	0.1270
JSRT	simulated X-rays	0.8759	0.6783	0.1234
JSRT	dual energy X-rays	0.7618	0.5823	0.1721
Montgomery	manually delineated	0.9519	0.8718	0.0941
Montgomery	simulated X-rays	0.9086	0.7962	0.1423
Montgomery	dual energy X-rays	0.7711	0.6067	0.1626

Table 1: Optimal points on ROC curve: Area Under Curve (AUC), optimal True Positive (TP) rate, and optimal False Positive (FP) rate.

format [36]. Therefore, the film-based images have a homogeneous intensity appearance. On the other hand, the X-rays in the Montgomery set were acquired using digital scanners. These images have much higher contrast with stronger rib-bone edges. The intensity variations are more heterogeneous compared to the JSRT dataset.

The curves also show that rib segmentation based on manually generated rib models (solid lines) are superior to rib segmentation based on models generated from simulated X-rays (dashed lines), and to rib segmentation based on dual energy bone images (dotted lines). We believe that the reason for the lower accuracy obtained with simulated X-ray is that the average intensity projection produces a smooth simulated X-ray that does not capture adequate texture information for similarity computation during the registration process (cf. Figure 4). Each X-ray of the Belarus dataset, which we used to compute the simulated X-rays, contains 128 axial slices. The simulated X-ray accuracy could be improved using CT scans with a higher number of slices. On the other hand, the lower accuracy obtained with dual energy X-ray images occurs due to overlapping bone structures in bone X-ray images, and weak bone intensity in mid-line region (Fig. 3-c). During registration of the model to the patient X-ray, the anterior rib structures and weak bone intensity deteriorated the posterior rib pixel estimation. We computed the optimal points on the ROC curves (showed as circles on curves in Figure 8) and listed the area under the curve, optimal TP and FP rates in Table 1.

4.3. Challenging X-rays

Rib-bone segmentation is challenging due to rib-bone variances across patients. Rib bone mineral density, respiration, body movement during X-ray capture and disease in the lung region affect the rib-bone shape and number of visible ribs. Fig 9 shows the performance of our system in these challenging situations.

The system is able to locate the ribs given adequate texture information for the rib region. We register the rib models to the patient X-ray using a non-rigid registration approach. Therefore, our system successfully addresses the rib-shape variance between patients. However, it can not detect the ribs when the intensity difference between rib region and intercostal areas are poor.

4.4. Comparison Results

Most studies have conducted subjective evaluations for their rib detection algorithms because of the lack of a reference
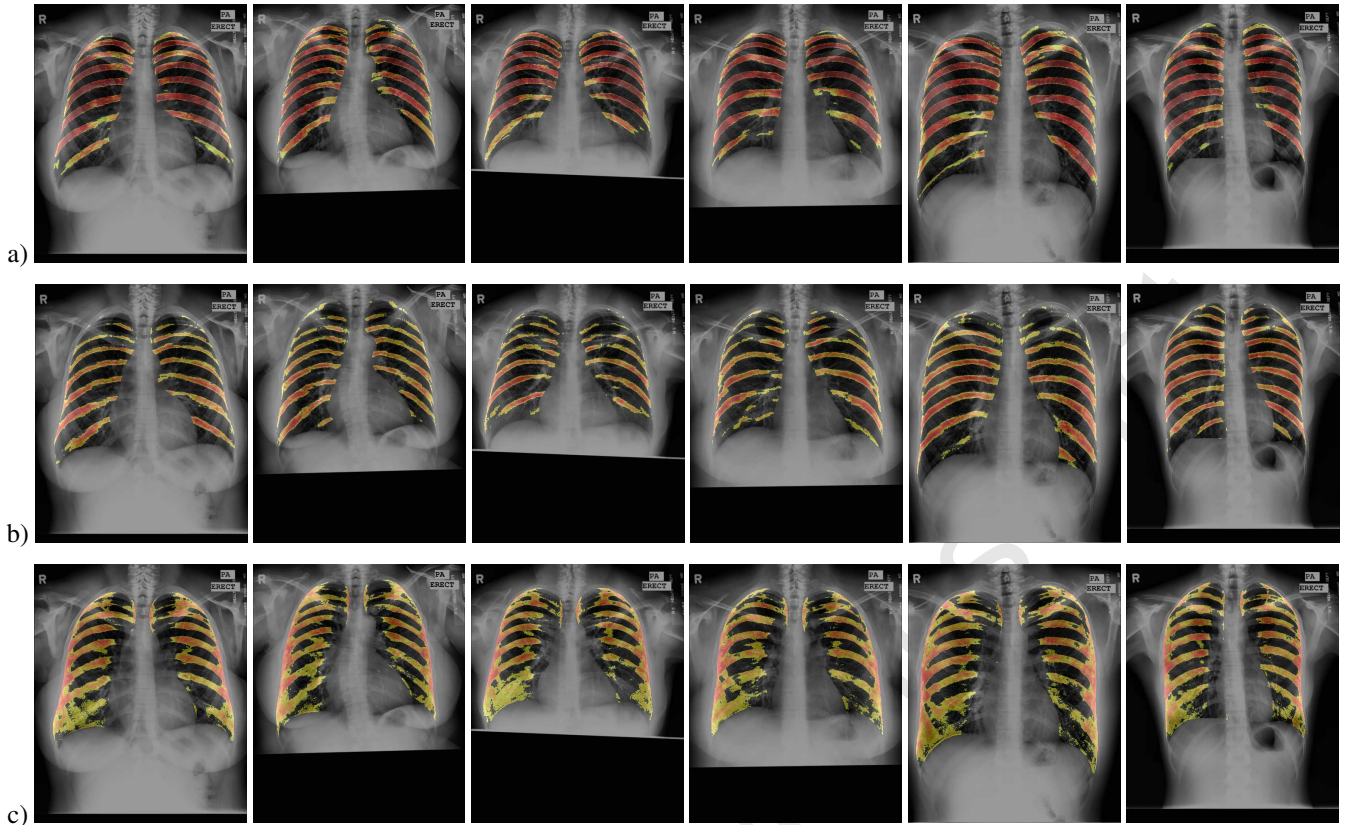
6

Figure 7: Example probability maps with a) manual atlas, b) atlas computed from CT scans, c) dual energy bone-tissue X-rays.
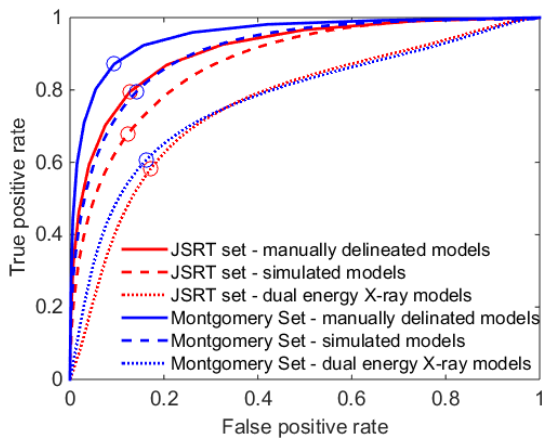

Figure 8: ROC curves for JSRT and Montgomery datasets, obtained with manually delineated rib-bone models, simulated models, and dual energy X-ray models.

boundary for quantitative evaluation. To the best of our knowledge, only [33] have reported quantitative results for rib detection on a public set (JSRT dataset). In order to compare the performance of our approach with the reported results in literature, we computed the rib boundary from the probability maps estimated for the JSRT dataset. The values on the probability map of each X-ray are between 0 to 1 (cf. Figure 6). We set a threshold for the map with $t = 0.5$, which is also the optimal threshold value in ROC curves. Table 2 lists the overall accuracy, sensitivity and specificity of algorithms. ICPC (iterated contextual pixel classification) uses pixel classification [33] as initial rib segmentation, and then re-classifies each pixel using image features and class labels of pixels in their neighborhood which are assigned in the initial segmentation. Pixel classification (PC) [33] classifies the ribs based on intensities and uses a supervised classification approach. The same authors proposed a model-based approach [30], which fits a global rib-bone model directly to the radiograph image. In the rib-bone model, each rib is represented by two parallel parabolas. However, this approach does not address the variable number of visible ribs in the lung area. Researchers also measured the human variance by comparing two manual delineations, which is listed as second observer performance. Our overall method performance on the JSRT subset is comparable with ICPC and close to the second observer performance. (Note that the experimental data subset is not the same because the authors in [33] did not disclose the specific subset used). Our approach uses both image
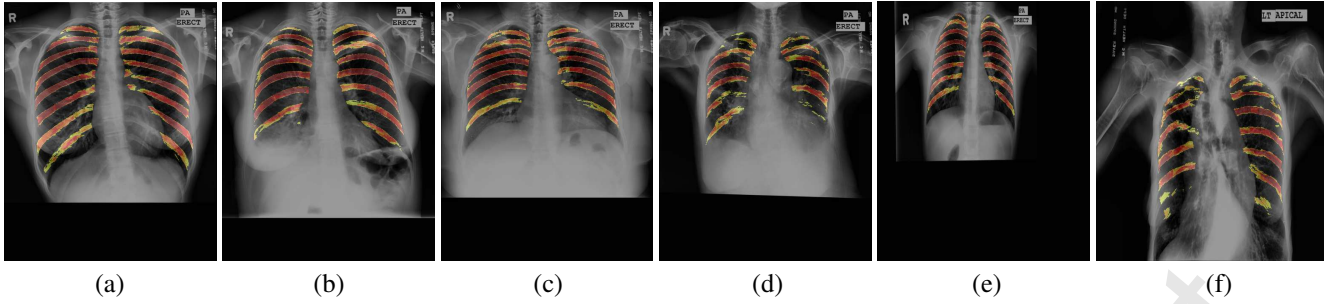
7

Figure 9: a) 8 visible ribs, slightly rotated body movement. b) 7 visible ribs on the left, 8 visible ribs on the right. c) 7 visible ribs, the rib intervals are narrow. d) Rotated body shape, deformed lung shape, poor contrast at the bottom part of lung. e) Rotated body shape, the lung size is smaller due to black border around the X-ray. f) Deformed lung shape due to disease.

information and a rib-bone model, therefore, it performs better than the PC method on the challenging cases.

Procedure	Accuracy	Sensitivity	Specificity
ICPC [33]	0.86 ± 0.06	0.79 ± 0.09	0.92 ± 0.04
PC [33]	0.79 ± 0.05	0.71 ± 0.08	0.85 ± 0.03
Model-based method [30]	0.74 ± 0.05	0.71 ± 0.08	0.85 ± 0.03
Second Observer [33]	0.94 ± 0.02	0.92 ± 0.03	0.95 ± 0.02
Our Method - with 10 model	0.84 ± 0.04	0.79 ± 0.06	0.87 ± 0.03
Our Method - with 15 model	0.85 ± 0.04	0.73 ± 0.06	0.92 ± 0.02
Our Method - with 20 model	0.86 ± 0.03	0.75 ± 0.06	0.92 ± 0.02

Table 2: Average Accuracy, Sensitivity and Specificity of Iterated Contextual Pixel Classification (ICPC) [33], Pixel Classification [33], a rule-based method [30], Human observer performance [33] and our method.

5. Conclusions

Here we propose an atlas-based system to extract the rib-bone boundary on conventional CXRs. Given a patient X-ray, the system first chooses the most similar models in the atlas set and then registers them to the patient X-ray. As atlas models, in addition to using manually delineated models, we propose two alternative atlases: (i) simulated models computed from CT scans, and (ii) bone-tissue images from dual energy machines. During the registration process, we compute the transformation mapping between the model X-ray and the patient X-ray by computing the regional similarities between the X-rays. Then, we apply the resulting transformation to the model rib-masks. The average of all registered models constitutes the rib bone probability map for the patient X-ray.

The proposed system builds the patient rib-bone model as a probability map in which each pixel intensity indicates the pixel's probability of being part of the rib-bone structure. In order to measure the performance of the system, we computed the ROC curves based on the computed probability maps. We achieved an AUC of approximately 95% for the Montgomery dataset and 91% for the JSRT dataset. To compute the rib boundaries, we set the threshold for the probability map with the threshold given by the optimal point on the ROC curve. We achieved 85% accuracy, 75% sensitivity, and 92% specificity on a public CXR set.

The probability maps and boundary results showed that the system successfully locates the rib-bones if there is adequate texture information. It successfully addresses the rib-shape variance between patients and the number of visible rib bones due to patient respiration. The algorithm produces relatively less accurate boundaries at the bottom part of the lung. This is due to the weak intensity difference between the rib-bone and soft tissue. The anterior ribs are not as clearly visible as posterior ribs on X-ray images. Therefore, our appearance-based approach could not detect the anterior ribs as accurately as the posterior ribs. We compared our findings with the algorithms in the literature by testing the algorithm on a public set. Our overall method performance is comparable with the state-of-the-art approach and close to human observer performance.

Appendix

The Montgomery dataset, as well as corresponding lung boundaries, is publicly available for research purposes. To submit the request, please visit the following webpage: https://ceb.nlm.nih.gov/repos/chestImages.php.

Acknowledgment

[1] National library of medicine, chest x-ray screening project, http://archive.nlm.nih.gov/repos/chestImages.php/, [Online; accessed 10-October-2013].

[2] S. Jaeger, A. Karargyris, S. Candemir, L. Folio, J. Sielgelman, F. Callaghan, Z. Xue, K. Palaniappan, R. Singh, S. Antani, G. Thoma, Y.-X. Xiang, P.-X. Lu, C. McDonald, Automatic tuberculosis screening using chest radiographs, IEEE Trans. on Medical Imaging 33 (2) (2014) 233–245.

[3] S. Candemir, S. Jaeger, K. Palaniappan, M. J.P., S. R.K., Z. Xue, A. Karargyris, S. Antani, G. Thoma, C. McDonald, Lung segmentation in chest radiographs using anatomical atlases with non-rigid registration, IEEE Trans. on Medical Imaging 33 (2) (2014) 577–590.

[4] X. Chen, K. Doi, S. Katsuragawa, H. MacMahon, Automated selection of regions of interest for quantitative analysis of lung textures in digital chest radiographs, Medical physics 20 (1993) 975.

[5] S. Katsuragawa, K. Doi, H. MacMahon, Detection and characterization of interstitial lung disease in digital chest radiographs, Medical physics 15 (1988) 311.

8

[6] S. Katsuragawa, K. Doi, H. MacMahon, Classification of normal and abnormal lungs with interstitial disease in chest images, Medical physics 16 (1989) 38.

[7] H. Ogul, B. Ogul, M. Agildere, T. Bayrak, E. Sumer, Eliminating rib shadows in chest radiographic images providing diagnostic assistance, Computer Methods and Programs in Biomedicine (2015) – doi:http://dx.doi.org/10.1016/j.cmpb.2015.12.006.
URL http://www.sciencedirect.com/science/article/pii/S0169260715003296

[8] K. Suzuki, H. Abe, F. Li, K. Doi, Suppression of the contrast of ribs in chest radiographs by means of massive training artificial neural network, in: Medical Imaging 2004, International Society for Optics and Photonics, 2004, pp. 1109–1119.

[9] M. Loog, B. van Ginneken, A. Schilham, Filter learning: application to suppression of bony structures from chest radiographs, Medical image analysis 10 (6) (2006) 826–840.

[10] Z. Yue, A. Goshtasby, L. Ackerman, Automatic detection of rib borders in chest radiographs, Medical Imaging, IEEE Transactions on 14 (3) (1995) 525–536.

[11] F. Plourde, F. Cheriet, J. Dansereau, Semiautomatic detection of scoliotic rib borders from posteroanterior chest radiographs, Biomedical Engineering, IEEE Transactions on 59 (4) (2012) 909–919.

[12] A. Frangi, D. Rueckert, J. Schnabel, W. Niessen, Automatic construction of multiple-object three-dimensional statistical shape models: Application to cardiac modeling, Medical Imaging, IEEE Transactions on 21 (9) (2002) 1151–1166.

[13] X. Artaechevarria, A. Munoz-Barrutia, C. Ortiz-de Solorzano, Combination strategies in multi-atlas image segmentation: Application to brain mr data, Medical Imaging, IEEE Transactions on 28 (8) (2009) 1266–1277.

[14] P. Aljabar, R. Heckemann, A. Hammers, J. Hajnal, D. Rueckert, Multi-atlas based segmentation of brain images: atlas selection and its effect on accuracy, Neuroimage 46 (3) (2009) 726–738.

[15] J. Lötjönen, R. Wolz, J. Koikkalainen, L. Thurfjell, G. Waldemar, H. Soininen, D. Rueckert, Fast and robust multi-atlas segmentation of brain magnetic resonance images, NeuroImage 49 (3) (2010) 2352–2365.

[16] T. F. Cootes, C. J. Taylor, D. H. Cooper, J. Graham, Active shape models - their training and application, Comput. Vis. Image Understand. 61 (1) (1995) 38–59.

[17] T. Cootes, G. Edwards, C. Taylor, Active appearance models, IEEE Trans. Pattern Anal. Mach. Intell. 23 (6) (2001) 681–685.

[18] I. Isgum, M. Staring, A. Rutten, M. Prokop, M. Viergever, B. Ginneken, Multi-atlas-based segmentation with local decision fusion: Application to cardiac and aortic segmentation in ct scans, Medical Imaging, IEEE Transactions on 28 (7) (2009) 1000–1010.

[19] F. Shi, P. Yap, Y. Fan, J. Gilmore, W. Lin, D. Shen, Construction of multi-region-multi-reference atlases for neonatal brain mri segmentation, Neuroimage 51 (2) (2010) 684–693.

[20] D. Collins, J. Pruessner, Towards accurate, automatic segmentation of the hippocampus and amygdala from mri by augmenting animal with a template library and label fusion, NeuroImage 52 (4) (2010) 1355–1366.

[21] A. Khan, N. Cherbuin, W. Wen, K. Anstey, P. Sachdev, M. Beg, Optimal weights for local multi-atlas fusion using supervised learning and dynamic information (superdyn): Validation on hippocampus segmentation, NeuroImage 56 (1) (2011) 126–139.

[22] T. Langerak, U. van der Heide, A. Kotte, M. Viergever, M. van Vulpen, J. Pluim, Label fusion in atlas-based segmentation using a selective and iterative method for performance level estimation (simple), Medical Imaging, IEEE Transactions on 29 (12) (2010) 2000–2008.

[23] M. Sabuncu, B. Yeo, K. Van Leemput, B. Fischl, P. Golland, A generative model for image segmentation based on label fusion, Medical Imaging, IEEE Transactions on 29 (10) (2010) 1714–1729.

[24] M. Murgasova, L. Dyet, D. Edwards, M. Rutherford, J. Hajnal, D. Rueckert, Segmentation of brain mri in young children, Academic radiology 14 (11) (2007) 1350–1366.

[25] G. Powell, K. Doi, S. Katsuragawa, Localization of inter-rib spaces for lung texture analysis and computer-aided diagnosis in digital chest images, Medical physics 15 (1988) 581.

[26] P. de Souza, Automatic rib detection in chest radiographs, Computer vision, graphics, and image processing 23 (2) (1983) 129–161.

[27] J. Lee, J. Wang, H. Wu, M. Yuan, A nonparametric-based rib suppression method for chest radiographs, Computers & Mathematics with Applica-

tions 64 (5) (2012) 1390–1399.

[28] H. Wechsler, J. Sklansky, Automatic detection of rib contours in chest radiographs, Ph.D. thesis, Citeseer (1975).

[29] S. Sarkar, S. Chaudhuri, Detection of rib shadows in digital chest radiographs, in: Image Analysis and Processing, Springer, 1997, pp. 356–363.

[30] B. van Ginneken, B. ter Haar Romeny, Automatic delineation of ribs in frontal chest radiographs, in: Medical Imaging 2000, International Society for Optics and Photonics, 2000, pp. 825–836.

[31] S. Sanada, K. Doi, H. MacMahon, Automated detection of pneumothorax in chest images, Medical physics 19 (1992) 1153.

[32] S. Benameur, M. Mignotte, F. Destrempes, J. De Guise, Three-dimensional biplanar reconstruction of scoliotic rib cage using the estimation of a mixture of probabilistic prior models, Biomedical Engineering, IEEE Transactions on 52 (10) (2005) 1713–1728.

[33] M. Loog, B. Ginneken, Segmentation of the posterior ribs in chest radiographs using iterated contextual pixel classification., IEEE Trans. Medical Imaging 25 (2006) 602–611.

[34] M. Gargouri, J. Tierny, E. Jolivet, P. Petit, E. Angelini, Accurate and robust shape descriptors for the identification of rib cage structures in ct-images with random forests, in: 2013 IEEE 10th International Symposium on Biomedical Imaging,, 2013, pp. 65–68.

[35] J. Shiraishi, S. Katsuragawa, J. Ikezoe, T. Matsumoto, T. Kobayashi, K. Komatsu, M. Matsui, H. Fujita, Y. Kodera, K. Doi, Development of a digital image database for chest radiographs with and without a lung nodule: receiver operating characteristic analysis of radiologists detection of pulmonary nodules, American Journal of Roentgenology 174 (2000) 71–74.

[36] B. Ginneken, M. Stegmann, M. Loog, Segmentation of anatomical structures in chest radiographs using supervised methods: a comparative study on a public database, Medical Image Analysis 10 (1) (2006) 19–40.

[37] Belarus tuberculosis portal, http://www.tuberculosis.by/, [Online; accessed 30-October-2014].

[38] V. Kovalev, V. Liauchuk, I. Safonau, A. Astrauko, A. Skrahina, A. Tarasau, Is there any correlation between the drug resistance and structural features of radiological images of lung tuberculosis patients?, Int J Comp Assist Radiol Surg 8 (1) (2013) 18–20.

[39] D. Beard, Firefly - web-based interactive tool for the visualization and validation of image processing algorithms, Master's thesis, University of Missouri (2009).

[40] P. Madala, Interactive web-based track editing and management, Master's thesis, University of Missouri (2011).

[41] Z. Xu, U. Bagci, C. Jonsson, S. Jain, D. Mollura, Efficient ribcage segmentation from ct scans using shape features, in: Engineering in Medicine and Biology Society (EMBC), 2014 36th Annual International Conference of the IEEE, 2014, pp. 2899–2902.

[42] C. Tomasi, R. Manduchi, Bilateral filtering for gray and color images, in: Computer Vision, 1998. Sixth International Conference on, IEEE, 1998, pp. 839–846.

[43] J. Canny, A computational approach to edge detection, Pattern Analysis and Machine Intelligence, IEEE Transactions on (6) (1986) 679–698.

[44] C. Liu, J. Yuen, A. Torralba, SIFT flow: Dense correspondence across different scenes and its applications., IEEE Trans. Pattern Anal. Mach. Intell. 33 (5).

[45] D. Lowe, Distinctive image features from scale-invariant keypoints, Int. J. Computer Vision 60 (2) (2004) 91–110.

[46] S. K. Warfield, K. H. Zou, W. M. Wells, Simultaneous truth and performance level estimation (staple): an algorithm for the validation of image segmentation, Medical Imaging, IEEE Transactions on 23 (7) (2004) 903–921.